Galvanically Coupled Intra-body Communications for Medical Implants: A Unified Analytic Model

Article *in* IEEE Transactions on Antennas and Propagation · July 2016
DOI: 10.1109/TAP.2016.2559519

3 authors:

Assefa Teshome
Victoria University Melbourne
14 PUBLICATIONS **49** CITATIONS
SEE PROFILE

Behailu Kibret
Monash University (Australia)
31 PUBLICATIONS **208** CITATIONS
SEE PROFILE

Daniel T. H. Lai
Victoria University Melbourne
124 PUBLICATIONS **946** CITATIONS
SEE PROFILE

This article has been accepted for publication in a future issue of this journal, but has not been fully edited. Content may change prior to final publication. Citation information: DOI 10.1109/TAP.2016.2559519, IEEE Transactions on Antennas and Propagation

Galvanically Coupled Intra-body Communications for Medical Implants: A Unified Analytic Model

Assefa K. Teshome, *Member, IEEE,* Behailu Kibret, *Member, IEEE,* and Daniel T. H. Lai, *Member, IEEE*

***Abstract*—Health-care monitoring and diagnostics technology continues to be of great interest in research due to an increasing trend in the number of people with chronic diseases. To improve accuracy and timeliness of diagnosis, electronic devices could be implanted inside human body to provide various real-time diagnostic information. However, effective technique for communicating the implant with outside world is still an open problem. Early efforts based on radio wave propagation are standardised as the Medical Implant Communication Services (MICS) for 402–405 MHz frequency range which was later adopted as Medical Devices Radiocommunications Services (MedRadio) for 401–406 MHz frequency range . Intra-body communication (IBC) is a relatively new technique that uses the human body as a channel with communication frequencies not exceeding several MHz. In this work, we propose a new analytical electromagnetic model that uses galvanically coupled IBC as an alternative to radio wave based implant communication. The model is unified in the sense that it is based on multi-layered ellipsoidal geometry that can be applied to any part of the body (i.e., head, torso, limbs etc.). Our model effectively describes influences of tissue layer thicknesses and electromagnetic properties, implant size and depth, and geometry of the body part. The model proves the security and low power consumption of IBC. The path loss characterisation of IBC implants shows lower values compared to their MICS counterparts.**

***Index Terms*—Medical implants, Intra-body communication, Galvanically coupled IBC, Electromagnetic model, Multilayered Ellipsoidal geometry.**

I. Introduction

RESEARCH in electronic health monitoring and medical diagnostics technology has attracted a large number of researchers from engineering and medical disciplines. In fact, it will continue even more so due to an increasing prevalence of chronic diseases [1]. To improve accuracy and timeliness of diagnosis, and hence improve quality of life, sophisticated actuators and biosensors are emerging for various diagnostic applications; for example, glucose sensors for continuous diabetes monitoring [2]. For real-time health care monitoring, these biosensors need to be implanted inside the respective organs and tissues. However; effective techniques for transmitting these quantities to the outside world is still an open problem. Over the past decades, several communication techniques have been proposed to enable communications of implanted devices; although, only a few have been implemented in existing implants such as cardiac pacemakers, deep-brain stimulators, gastric defibrillators etc.

In 1999, the European Telecommunications Standards Institute (ETSI) standardized previous efforts as what is often referred to as the MICS standard. This standard uses radio wave propagation based wireless Radio Frequency (RF) communication occupying bandwidths of 300 kHz in the frequency range 402–405 MHz [3]. Later in 2009, the Federal Communications Commission (FCC) adopted the Medical Device Radiocommunications Service (MedRadio) in the 401–406 MHz range by combining the existing MICS band as the MedRadio core and the spectrum at 401–402 MHz and 405–406 MHz as MedRadio wing [4]. In addition, other wideband radio wave based techniques in GHz range and techniques using inductively coupled transmission have also been studied and advantages and challenges associated are discussed in [5–7]. For implant communication, electromagnetic waves at such high frequencies need to travel through various tissues of human body where signals suffer a great deal of attenuation. Thus, large power is required for transmission which results in an expensive powering regime including frequent replacement of battery in battery powered implants. Moreover, transmission power within human tissues is limited by safety recommendations of Specific Absorbtion Rate (SAR) levels by the International Commission on Non-Ionizing Radiation Protection (ICNIRP) [8].

Pioneered by the early works of Zimmermann conducted in 1995 [9], intra-body communications at a much lower frequency compared to their MedRadio counterparts have gained a spotlight in the research community. Relatively recently, in 2012, the IEEE 802.15.6 work group released standards for intra-body communications. Intra-body communication (IBC) and Human body communication (HBC) are terms used interchangeably to refer to electric field communication (EFC) using the human body as a channel as a result of electric current, with frequencies ranging from a couple of hundreds of kHz to a few tens of MHz, injected through electrodes of the transmitter [10]. In addition to the HBC layer, the IEEE 802.15.6 standard includes the MedRadio band and the industrial, scientific and medical (ISM) band (2.4 GHz) in its narrow band (NB) and ultra-wideband (UWB) layers respectively. In the case of HBC, the signal can be coupled capacitively where only the signal electrode is connected to human body with the ground electrode left floating [9], or galvanically where both the signal and ground electrodes are connected to human body to inject current differentially[11]. The standard, however, focuses more on the use of HBC for surface-to-surface communication.

In this work, we propose a new analytical model for the use of galvanically coupled intra-body communication technique as an alternative for implant communication. For implant communication, since the transmitter is implanted in the body, it is important that it consumes small power to conserve battery

All authors are with the College of Engineering and Science, Victoria University, Melbourne, VIC 3011 Australia, e-mail: assefa.teshome@live.vu.edu.au.

This article has been accepted for publication in a future issue of this journal, but has not been fully edited. Content may change prior to final publication. Citation information: DOI 10.1109/TAP.2016.2559519, IEEE Transactions on Antennas and Propagation

life. Besides, due to sensitive nature of medical data, it is imperative that security is a paramount requirement of implant communication. To achieve security either the signal needs to be encrypted at the transmitter or be confined to within the body detectable only by on-body receiver.

In the case of MedRadio based implant, the signal is radiated outside the human body; hence, requires all security features be implemented right at the transmitter which increases the transmitter complexity. Hence, the transmitter consumes large power and is difficult to miniaturise.

HBC uses an electric field communication (EFC) where the human body is effectively a volume conductor. It uses the lossy dielectric nature of the conductive tissue layers to induce a current, and hence a potential distribution, as a result of the electric field caused by the current injected by the transmitter electrode(s). Such a low frequency signal is expected to penetrate deeper into the tissue layers, thus requiring less power be detected by a receiver on the surface of skin. Moreover, due to a non conducting free space outside the skin surface, the signal is confined to within the human body (i.e., inherently secure).

Lindsay *et al.* [12] used galvanically coupled implant communication between skin surface and a sensor implanted in anterior cruciate ligament of a cadaver in an experimental setting. They have empirically observed a minimum path loss of 37 dB for signals with frequency 2–160 kHz and currents of 1–3 mA at 5 cm distance from the transmitter location. Sun *et al* [13] used a simplified homogenous spherical model and implemented an implant to surface transmitter. They successfully introduced 'x' – shaped electrodes to improve current flow and hence minimise power consumption significantly [14]. However, the discrepancy between the simplified model and the actual measured values show that homogenous models overestimate the measured surface potential which requires a proper multilayered tissue model. Wegmuler *et al* [15] implemented a finite element method (FEM) simulation of implant–to–implant communication and conducted an experimental test on a homogenous phantom solution. They used signals at 100–500 kHz with current less than 1 μA and found approximately 32 dB loss over 5 cm of transmission distance. Their work reported the predicted dependency of path loss with transmission distance and electrode length. Other mechanisms of implant-able wireless communication and their challenges are also reviewed in [1], [16], [17].

Since it is difficult to conduct *in vivo* measurements in living humans, to characterise implant communication, experiments have been limited to human cadaver [12] (a different channel due to dry tissues and dead blood cells), anesthetized animals and homogenous body phantom solutions [13]. On the other hand, the existing numerical and analytical models for implant communication are limited to homogenous volumes of simplified geometries [15]. Implant location directly affects communications due to path loss variation resulting from anthropometric geometries and tissue strata dimensions. Little has been reported on characteristics of different parts of human body as a channel for implant communication. Our proposed model provides analytical solution to a volume conduction based implant communication scenario for any part of the body modelled as multilayered ellipsoidal geometry.

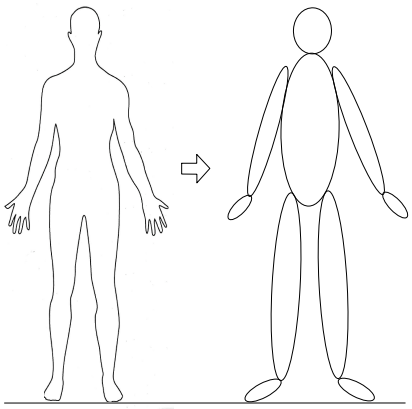

Fig. 1: Ellipsoidal approximation of human body

The reminder of this paper is organised as follows: Section II motivates and discusses the framework of our model setup while Section III briefly describes the volume conduction theory and restates the set of Maxwell's equations that govern a galvanically coupled implant communication under quasi-static assumptions. In Section IV, we define the confocal multilayered ellipsoidal geometry and its symmetry associated with various tissue layers. Later, Section V presents the derivation of electric potential distribution by treating special functions called Lamé's functions in an ellipsoidal coordinate system. Section VI discusses the results in view of potential distribution, path loss and effect of tissue layers; and finally our conclusion is given in Section VIII.

II. Model Setup

In literature, several modeling techniques have been used to model the human body as a channel. Some of these techniques include the two-terminal circuit model [18], [19], four-terminal circuit model [19], [20], finite element approach [15], [21], surface electromagnetic propagation models [22], [23], near-field electromagnetic models [23] and quasi-static electromagnetic models [24]. Each model show various useful aspects of intra-body communication. However, the electromagnetic models used are based on simple geometries which limit their use to only specific regions of the body. On the other hand, circuit models are generally shortsighted in the sense that the relationship between channel variations and circuit components is not obvious in the transfer functions, albeit well characterized channels in fixed settings.

In this work, we presented an analytical electromagnetic model motivated by geometries robust enough to capture tissue layer effects in a scalable way that can be applied to any part of the body and yet simple enough to guarantee analytical solutions. Based on this geometry, we derive a mathematical model of the channel and characterise the received signal as a function of the size of the transmitter, tissue layers of the body part, transmitter location (depth of implantation), receiver location and electrode spacing.

Looking at the human body anatomy, we find most body parts can be approximated by a variation of an ellipsoidal geometry as shown in Fig. 1. A spherical, prolate spheroid,

This article has been accepted for publication in a future issue of this journal, but has not been fully edited. Content may change prior to final publication. Citation information: DOI 10.1109/TAP.2016.2559519, IEEE Transactions on Antennas and Propagation

oblate spheroid, or ellipsoid with a dominating semi-axis are several derivatives of an ellipsoidal geometry that can describe various parts of the human body. The human head can be modelled using an ellipsoid close to spherical symmetry. The torso can be modeled by a prolate or oblate spheroid versions of the ellipsoidal geometry. Limbs can be modelled by an ellipsoid where a dominating semi-axis represents the limb length whereas the other two axes represent the larger and the shorter radii of the limb. When one of the semi-axes is large and the other two are comparable, the geometry resembles a cylinder which is often used in existing electromagnetic models e.g. [24], [21].

Hence, an analytical model based on multilayered ellipsoidal representation of tissue layers can represent the various body parts by defining the semi-axes lengths. The ellipsoidal shells in the layers represent each tissue layer with varying thickness and complex permittivity. As we will see in Section V, the orthogonal property of the ellipsoidal harmonics and the symmetry of the ellipsoidal geometry allows us to simplify complex mathematical expressions that might result otherwise. Ellipsoidal geometry and harmonics have been successfully used in gravitational field analysis in astronomy to represent celestial objects in solar system [25], and in the inverse problem of brain activity source localisation of Electroencephalography (EEG) [26] and Magnetoencephalography (MEG) [27].

III. Volume Conduction Theory for Implant Communication

Volume conduction can be defined as a transmission technique for electric field inside the volume of a lossy dielectric where an electric field is induced by a primary current source; and this field propagates to the receiver by means of an induction current induced in the conductive medium [28]. An implant transmitter coupled galvanically can be envisaged as the primary current source inside one or more lossy layers of body tissue. The total current inside the volume (i.e., primary and induction currents added) creates an electric potential distribution inside and on the surface of the volume [29]. The receiver could be either another implant or on-body device where its two electrodes are used to sample the potential difference between the two points of the body the electrodes are connected to. The transmission frequencies we consider are smaller than the high frequency band of the spectrum. From the conductivity and permittivity profiles of human body tissues at these small frequencies, electromagnetic signals in the body can be assumed to be quasi-static [24], [30]. In quasi-static assumptions, the variations of electric and magnetic fields, denoted as $\mathbf{E}$ and $\mathbf{B}$ respectively, with time are negligible. Hence, the set of Maxwell's equation describing the fields inside the human body can be modified as follows:

$$\begin{aligned} \nabla \times \mathbf{E} &= 0, & \nabla \times \mathbf{B} &= \mu J, \\ \nabla \cdot \mathbf{E} &= 0, & \nabla \cdot \mathbf{B} &= 0. \end{aligned} \tag{1}$$

Where μ is permeability of free space and $\mathbf{J}$ is the net current density in side the volume. Here, the electric field $\mathbf{E}$ is

$$\mathbf{E} = -\nabla V, \tag{2}$$

where V is the electric potential distribution.

The galvanically coupled implant transmitter, as shown in Fig. 2, is modelled such that its two electrodes are acting as a source and a sink for the primary current injected into the volume. Denote the source point in three dimensional space by r_1 and the sink by r_2. We consider these two points as points of singularity where the current can be expressed as a point current source. The source density $[A/m^3]$ at the source point is expressed as $I_{source}(r) = I\delta(r - r_1)$ and the current density at the sink is $I_{sink}(r) = -I\delta(r - r_2)$ where I is the primary current $[A]$ injected by the transmitter. Here, assuming no other current sources, the net source current density I_{tot} injected, as a function of point r in space, is given by

$$I_{tot}(r) = I[\delta(r - r_1) - \delta(r - r_2)]. \tag{3}$$

The assumption that there are no other current sources is further supported by the fact that we are operating at frequencies well above human bio-signal frequencies which are limited to 10 kHz [31].

The nature of the current distribution creates a current dipole moment acting midway between the source and the sink given by $\mathfrak{M} = Id$ where $d = |r_1 - r_2|$ is the electrode spacing. As a result, the net primary current source density J^s is

$$J^s(r) = \mathfrak{M}\delta(r - r_0) \tag{4}$$

where $r_0 = \frac{r_2+r_1}{2}$ is the mid point between the source and sink which the current dipole is acting on. This source current induces the electric field $\mathbf{E}$ given in (2). The field $\mathbf{E}$ in turn induces a current known as induction current. The current density J^i of this induction current is

$$J^i(r) = \sigma(r)\mathbf{E}(r) \tag{5}$$

where $\sigma(r)$ is the conductivity of the tissue layer at point r. The net current density J inside the volume is then

$$\begin{aligned} J(r) &= J^s(r) + J^i(r) \\ &= J^s(r) + \sigma(r)\mathbf{E}(r). \end{aligned} \tag{6}$$

It is this net current density J that propagates the signal from the transmitter to a receiver implanted inside the body or on the skin surface. Taking the divergence on both sides of (6), we have

$$\nabla \cdot J(r) = \nabla \cdot J^s(r) + \nabla \cdot \sigma(r)\mathbf{E}(r). \tag{7}$$

For implant communication, the region outside the volume under consideration is non conducting air (i.e., $\sigma(r) = 0$). Therefore, it is evident that the electric current is confined to within the body and no amount of electric current diverges outside the human body. Hence, the divergence of the current density $\nabla \cdot J = 0$. As a result, from (7) we have

$$-\nabla \cdot \sigma(r)\mathbf{E}(r) = \nabla \cdot J^s(r). \tag{8}$$

Substituting (2) and (4) into (8), we have

$$\nabla \cdot \sigma(r)\nabla V(r) = \nabla \cdot \mathfrak{M}\delta(r - r_0). \tag{9}$$

From (9), we can see that the potential distribution follows Poisson's equation inside the layer the implant is embedded in. However, for the rest of the tissue layers that do not

This article has been accepted for publication in a future issue of this journal, but has not been fully edited. Content may change prior to final publication. Citation information: DOI 10.1109/TAP.2016.2559519, IEEE Transactions on Antennas and Propagation

contain the implant, i.e., where J^s vanishes, the potential distribution follows Laplace's equation. Interestingly, from an analytical view point, the primary current propagates through various layers of tissue through the Neumann and Dirichlet boundary conditions at the interfaces between each tissue layers. The Neumann and the Dirichlet boundary conditions for this problem can be interpreted as the continuity of current density and electric potential at each interface. To solve for the potential V using (9), we need to specify the geometry and the set of boundary conditions for the problem. In our model, layers of body tissue are represented by multiple confocal ellipsoidal geometry defined in the following section.

IV. Ellipsoidal Geometry and Its Symmetry

An ellipsoid is a 3D object defined in Cartesian coordinates as [32]

$$\frac{x^2}{\alpha_1^2}+\frac{y^2}{\alpha_2^2}+\frac{z^2}{\alpha_3^2}=1 \text{ with } \alpha_1>\alpha_2>\alpha_3>0, \tag{10}$$

where α_1, α_2 and α_3 are the semi-axes in the x, y and z directions of the Cartesian coordinate respectively. We use the ellipsoid given in (10) as a basis ellipsoid to span confocal ellipsoids; accordingly, for any $\theta \in \mathbb{R}$ such that $\theta > -\alpha_3^2$, confocal layers of ellipsoids can be defined as

$$\frac{x^2}{\alpha_1^2+\theta}+\frac{y^2}{\alpha_2^2+\theta}+\frac{z^2}{\alpha_3^2+\theta}=1. \tag{11}$$

Let h_1, h_2 and h_3 be the differences between squares of the semi-axes (often referred to as semi-axes distances [26])

$$\begin{aligned} h_1^2&=\alpha_2^2-\alpha_3^2,\\ h_2^2&=\alpha_1^2-\alpha_3^2,\\ h_3^2&=\alpha_1^2-\alpha_2^2. \end{aligned} \tag{12}$$

For all confocal ellipsoids, we see that h_1, h_2 and h_3 are constant. Substituting $\lambda^2 = \alpha_1^2+\theta$ and (12) in (11), the confocal ellipsoidal expression becomes

$$\frac{x^2}{\lambda^2}+\frac{y^2}{\lambda^2-h_3^2}+\frac{z^2}{\lambda^2-h_2^2}=1. \tag{13}$$

For fixed x, y and z, (13) is a cubic equation in λ^2. If the corresponding three roots λ_1^2, λ_2^2 and λ_3^2 of (13) are such that $\lambda_1^2 > h_2^2 > \lambda_2^2 > h_3^2 > \lambda_3^2 > 0$, then $(\lambda_1, \lambda_2, \lambda_3)$ are the ellipsoidal coordinates corresponding to (x, y, z) in the Cartesian coordinate system. Points in the ellipsoidal coordinate system are formed by intersection of an ellipsoid ($\lambda_1 = Constant$), hyperboloid of one sheet ($\lambda_2 = Constant$) and hyperboloid of two sheets ($\lambda_3 = Constant$).

In this work, various tissue layers are modelled by confocal ellipsoids. This choice reasonably captures the convex interfaces and strict containment of volumes in the hierarchy of tissue layers except for limb joints. As such, interfaces are effectively modeled by one geometry. In addition, use of confocal ellipsoids helps us invoke the ellipsoidal symmetry to easily handle parameter changes in the resulting mathematical expressions. For a specific body part the semi-axes distances can be determined from the exterior geometry. Then, for each tissue layer, we need only adjust the value of λ (and consequently the semi-axes lengths) according to the corresponding tissue layer to define different body parts.

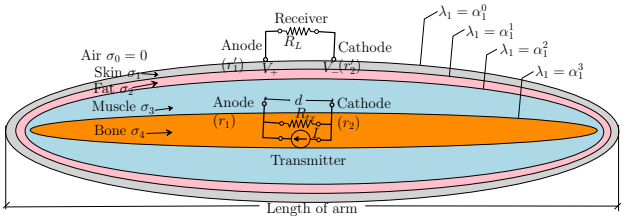

Fig. 2: Longitudinal cross-section of multilayered ellipsoidal model of human arm.

The Cartesian coordinate system is also used to define the implant transceiver location. The conversion from ellipsoidal coordinates to Cartesian coordinates is given by [25]

$$\begin{aligned} x^2&=\frac{\lambda_1^2\lambda_2^2\lambda_3^2}{h_2^2h_3^2},\\ y^2&=\frac{(\lambda_1^2-h_3^2)(\lambda_2^2-h_3^2)(h_3^2-\lambda_3^2)}{h_1^2h_3^2},\\ z^2&=\frac{(\lambda_1^2-h_2^2)(\lambda_2^2-h_2^2)(h_2^2-\lambda_3^2)}{h_1^2h_2^2}. \end{aligned} \tag{14}$$

Note here that unless signs are adjusted based on which octant the point falls in the ellipsoidal coordinate, the mapping from ellipsoidal to Cartesian coordinate system is many-to-one.

Consider the scenario where an implant transmitter is implanted inside the muscle tissue layer of human arm where a wearable device on the surface of the skin is used to receive the transmission. In this case, the human arm can be modeled with four confocal ellipsoids defined by $\lambda_1 = \alpha_1^i, \forall i \in \{0, 1, 2, 3\}$ as shown in Fig. 2. Here, Fig. 2 shows the longitudinal cross-section of the human arm with the four confocal ellipsoidal shells representing skin, fat, muscle and bone tissue layers with conductivities $\sigma_1, \sigma_2, \sigma_3$, and σ_4 respectively. The anode and the cathode electrodes of the transmitter are located at points r_1 and r_2 respectively. These points are specified in the three dimensions of the Cartesian coordinates system; we used (14) to calculate the corresponding ellipsoidal coordinates. Similarly, r_1' and r_2' denote locations of the anode and the cathode on the receiver side. The transmitter injects current I via the anode; the cathode, separated from the anode by an electrode spacing d, is a current sink.

Now that we have specified the geometric framework of our model, in the next section we will solve for the potential equation (9) using this framework.

V. Potential Distribution in Multilayered Confocal Ellipsoidal Harmonics

Solving for the electric potential requires solving the poisons equation in multilayered ellipsoidal geometry with the underlying boundary conditions at the interfaces between tissue layers and on the outer surface. Geslowitz *et al* [33] used Green's function to express the potential distribution at the outer surface and Lynn *et al* [34] used a Fredholm type integral equation to solve for potential. However, due to the singularity

This article has been accepted for publication in a future issue of this journal, but has not been fully edited. Content may change prior to final publication. Citation information: DOI 10.1109/TAP.2016.2559519, IEEE Transactions on Antennas and Propagation

of the kernel function for the electrostatic fields, analytical solutions do not exist. Hence, a multiple Weilandt deflation is applied to transform the kernel into a nonsingular type and a Jacobian recursive technique is used to find the potential distribution corresponding to the deflated kernel. Applying an appropriate correction factor, the potential distribution for the actual scenario can be computed in a semi-analytic numerical framework. Dechambre [25] and Kutori [26] on the other hand used separation of variables to solve for gravitational and electric fields respectively.

In this work, we use separation of variables in ellipsoidal coordinate systems to solve for the electric potential distribution at the receiver electrodes. Using the confocal ellipsoidal layers, we defined volumes of ellipsoidal shells to model tissue layers. Here, the potential distribution in each tissue layer not containing the transmitting implant (the current source) satisfies a Laplace's equation; whereas, the tissue layer containing the transmitter satisfies a Poisson's equation.

A. Laplace's Equation in Ellipsoidal Coordinates

Laplace's equation in Cartesian coordinates is given by

$$\frac{\partial^2 V}{\partial x^2}+\frac{\partial^2 V}{\partial y^2}+\frac{\partial^2 V}{\partial z^2}=0. \tag{15}$$

Using (14), Laplace's equation in ellipsoidal coordinates is

$$\frac{\partial}{\partial\lambda_1}\frac{H_1}{H_2H_3}\frac{\partial V}{\partial\lambda_1}+\frac{\partial}{\partial\lambda_2}\frac{H_2}{H_1H_3}\frac{\partial V}{\partial\lambda_2}+\frac{\partial}{\partial\lambda_3}\frac{H_3}{H_1H_2}\frac{\partial V}{\partial\lambda_3}=0, \tag{16}$$

where

$$\frac{H_1}{H_2H_3}=\sqrt{\frac{(\lambda_2^2-\lambda_3^2)^2(\lambda_1^2-h_3^2)(\lambda_1^2-h_2^2)}{(\lambda_2^2-h_3^2)(h_2^2-\lambda_2^2)(h_3^2-\lambda_3^2)(h_2^2-\lambda_3^2)}},$$
$$\frac{H_2}{H_1H_3}=\sqrt{\frac{(\lambda_1^2-\lambda_3^2)^2(\lambda_2^2-h_3^2)(h_2^2-\lambda_2^2)}{(\lambda_1^2-h_3^2)(\lambda_1^2-h_2^2)(h_3^2-\lambda_3^2)(h_2^2-\lambda_3^2)}},$$
$$\frac{H_3}{H_1H_2}=\sqrt{\frac{(\lambda_1^2-\lambda_2^2)^2(h_3^2-\lambda_3^2)(h_2^2-\lambda_3^2)}{(\lambda_1^2-h_3^2)(\lambda_1^2-h_2^2)(\lambda_2^2-h_3^2)(h_2^2-\lambda_2^2)}}.$$

To solve (16), the method of variable separation is used. In separating the three variables, we are looking for an expression of the potential of the form

$$V(\lambda_1,\lambda_2,\lambda_3)=\mathcal{R}(\lambda_1)\mathcal{M}(\lambda_2)\mathcal{N}(\lambda_3). \tag{17}$$

where $\mathcal{R},\mathcal{M}$ and $\mathcal{N}$ are functions only of λ_1,λ_2 and λ_3 respectively. Due to the fact that $\mathcal{R},\mathcal{M}$ and $\mathcal{N}$ are functions in each orthogonal axis such solution as (17) is known as a normal solution. Substituting (17) into (16) we can arrive at

$$(\lambda_2^2-\lambda_3^2)\phi_1(\lambda_1)+(\lambda_1^2-\lambda_3^2)\phi_2(\lambda_2)+(\lambda_1^2-\lambda_2^2)\phi_3(\lambda_3)=0 \tag{18}$$

where

$$\phi_1(\lambda_1)=\frac{\sqrt{(\lambda_1^2-h_3^2)(\lambda_1^2-h_2^2)}}{\mathcal{R}(\lambda_1)}\times\frac{d}{d\lambda_1}\Big(\sqrt{(\lambda_1^2-h_3^2)(\lambda_1^2-h_2^2)}\frac{d\mathcal{R}}{d\lambda_1}\Big),$$
$$\phi_2(\lambda_2)=\frac{\sqrt{(\lambda_2^2-h_3^2)(\lambda_2^2-h_2^2)}}{\mathcal{M}(\lambda_2)}\times\frac{d}{d\lambda_1}\Big(\sqrt{(\lambda_2^2-h_3^2)(\lambda_2^2-h_2^2)}\frac{d\mathcal{M}}{d\lambda_2}\Big),$$
$$\phi_3(\lambda_3)=\frac{\sqrt{(h_3^2-\lambda_3^2)(h_2^2-\lambda_3^2)}}{\mathcal{N}(\lambda_3)}\times\frac{d}{d\lambda_1}\Big(\sqrt{(h_3^2-\lambda_3^2)(h_2^2-\lambda_3^2)}\frac{d\mathcal{N}}{d\lambda_3}\Big).$$

Here, (18) is defined for any triplet $(\lambda_1,\lambda_2,\lambda_3)$ and it can easily be shown that $\phi_i(\lambda_i),\ \forall i\in\{1,2,3\}$ has a form $\phi_i(\lambda_i)=H\lambda_i^2-K$ for some constants H and K. Substituting this into (18), we have

$$(H\lambda_1^2-K)\mathcal{R}(\lambda_1)=\sqrt{(\lambda_1^2-h_3^2)(\lambda_1^2-h_2^2)}\times\frac{d}{d\lambda_1}\Big(\sqrt{(\lambda_1^2-h_3^2)(\lambda_1^2-h_2^2)}\frac{d\mathcal{R}}{d\lambda_1}\Big). \tag{19}$$

Equation (19) can be rewritten as

$$(\lambda_1^2-h_3^2)(\lambda_1^2-h_2^2)\frac{d^2\mathcal{R}(\lambda_1)}{d\lambda_1^2}+\lambda_1(2\lambda_1^2-h_3^2-h_2^2)\frac{d\mathcal{R}(\lambda_1)}{d\lambda_1}+(H\lambda_1^2-K)\mathcal{R}(\lambda_1)=0. \tag{20}$$

The differential equation given in (20) is known as Lamé's equation. Similarly, $\mathcal{M}(\lambda_2)$ and $\mathcal{N}(\lambda_3)$ also satisfy the Lamé's equation with respect to λ_2 and λ_3 respectively.

B. Lamé's Function to Describe Potential in Tissue Layers

Choosing the separation variables H and K carefully, the solutions to Lamé's equation can be forced to fall in to a set of the possible types of Lamé's functions of first kind of degree n and order p (given in Appendix A) denoted by E_n^p. For a given degree n, the order p takes values from the set $\{1,2,...,2n+1\}$; hence, there are a total of $(2n+1)$ Lamé's function of first kind. Note here that since all $\mathcal{R},\mathcal{M}$ and $\mathcal{N}$ satisfy the Lamé's equation, the product $E_n^p(\lambda_1)E_n^p(\lambda_2)E_n^p(\lambda_3)$ is also a normal solution of (16) according to (17). This product is continuous inside an ellipsoid and is simply denoted as $\mathbb{E}_n^p(\lambda_1,\lambda_2,\lambda_3)=E_n^p(\lambda_1)E_n^p(\lambda_2)E_n^p(\lambda_3)$.

Hence, inside an ellipsoid of larger semi-axis $\lambda_1=\alpha_1$, containing no current source, the electric potential distribution can be expressed as a linear combination of all possible Lamé's products and is given by

$$V(\lambda_1,\lambda_2,\lambda_3)=\sum_{n=0}^{\infty}\sum_{p=1}^{2n+1}\frac{\beta_n^p}{E_n^p(\alpha_1)}\mathbb{E}_n^p(\lambda_1,\lambda_2,\lambda_3) \tag{21}$$

where the coefficients $\frac{\beta_n^p}{E_n^p(\alpha_1)}$ are constant multipliers for each order and degree. Completion of the particular solution requires specifying potential equations and the coefficients in each tissue layer starting from the transmitter all the way

This article has been accepted for publication in a future issue of this journal, but has not been fully edited. Content may change prior to final publication. Citation information: DOI 10.1109/TAP.2016.2559519, IEEE Transactions on Antennas and Propagation

up to the receiver. Equation (21) is only used to describe the potential for the interior of the ellipsoid. However, we also need an expression for the exterior of the ellipsoid to completely describe the potential distribution. We see that $\lim_{\lambda_1\to\infty} E_n^p(\lambda_1) = \infty$; however, this contradicts the fact that the potential vanishes at infinity. Therefore, we need to find an other Lamé's function $F_n^p(\lambda_1)$ which still is a solution to Lamé's equation but vanishes at infinity. For an elliptic integral $I_n^p(\lambda_1)$ of order n and degree p given by

$$I_n^p(\lambda_1) = \int_{\lambda_1}^{\infty} \frac{dt}{(E_n^p(t))^2\sqrt{(t^2-h_2^2)(t^2-h_3^2)}},$$

a possible choice that satisfies both these requirement is [25]

$$F_n^p(\lambda_1) = (2n+1)E_n^p(\lambda_1)I(\lambda_1),$$

which is known as Lamé's function of second kind. Since $F_n^p(\lambda_1)$ satisfies the Laplace's equation and vanishes at infinity, the exterior potential for $\lambda_1 \geq \alpha_1$ can be expressed as

$$V(\lambda_1,\lambda_2,\lambda_3) = \sum_{n=0}^{\infty}\sum_{p=1}^{2n+1} \frac{\beta_n^p}{F_n^p(\alpha_1)}\mathbb{F}_n^p(\lambda_1,\lambda_2,\lambda_3) \qquad (22)$$

where $\mathbb{F}_n^p(\lambda_1,\lambda_2,\lambda_3) = F_n^p(\lambda_1)E_n^p(\lambda_2)E_n^p(\lambda_3)$. It can be shown that the products $E_n^p(\lambda_2)E_n^p(\lambda_3)$, referred to as ellipsoidal harmonics, are orthogonal up to a normalisation factor [26]; i.e., over the surface S_λ of an ellipsoid given by $\lambda_1 = \lambda$,

$$\int_{S_\lambda} \frac{E_n^p(\lambda_2)E_n^p(\lambda_3)E_{\acute{n}}^{\acute{p}}(\lambda_2)E_{\acute{n}}^{\acute{p}}(\lambda_3)}{\sqrt{(\lambda^2-\lambda_2^2)(\lambda^2-\lambda_3^2)}}dS = 0, \forall n \neq \acute{n} \text{ or } p \neq \acute{p}$$

$$\text{and } \int_{S_\lambda} \frac{(E_n^p(\lambda_2)E_n^p(\lambda_3))^2}{\sqrt{(\lambda^2-\lambda_2^2)(\lambda^2-\lambda_3^2)}}dS = \gamma_n^p. \qquad (23)$$

where γ_n^p is the normalisation constant. The orthogonality property in (23) is essential in determining the coefficients of the potential in the region which contains the singularity points. Expressions of $E_n^p(\lambda_i)$ and $\gamma_n^p, \forall n \leq 3$ are given in Appendices A and B respectively.

C. Boundary Conditions and Explicit Potential Distribution

So far, we have the general expressions for the interior and exterior ellipsoidal potentials. In the following we will derive the explicit expression of the potential distribution for the scenario given in Fig. 2. There are four tissue layers and air as the external medium. For signals with frequency $\omega = 2\pi f$, the complex permittivity at location r is $\epsilon(r) = \epsilon_r(r)\epsilon_0$, and the complex conductivity $\sigma(r) = i\omega\epsilon_0\epsilon_r(r)$ where ϵ_0 is the permittivity of free space and relative permittivity $\epsilon_r(r)$ is given by the Cole-Cole equation as

$$\epsilon_r(r) = \epsilon_\infty(r) + \sum_{m=1}^{4} \frac{\Delta\epsilon_m(r)}{1+(i\omega\tau_m(r))^{(1-\alpha_m(r))}} + \frac{\sigma_j(r)}{i\omega\epsilon_0}. \qquad (24)$$

Here, the parameters $\epsilon_\infty(r), \Delta\epsilon_m(r), \sigma_j(r), \alpha_m(r), \tau_m(r)$ such that $\epsilon_r(r)$ fits the experimental measurements of Gabriel *et al* [35] can be referred from the IT'IS website [36].

Inside each layer $i \in \{0,1,2,3,4\}$ (i.e., air, skin, fat, muscle and bone), the complex conductivity $\sigma(r)$ is assumed to be constant. Thus, $\sigma(r) = \sigma_i$, if $r \in i^{th}$ layer. Let the potentials in tissue layer with complex conductivity σ_i be denoted by V_i, $\forall i \in \{0,1,2,3,4\}$. Current induced in each tissue layer creates potential distribution and also affects the potential distribution of exterior layers. Thus, the net potential distribution is the sum of of the interior and exterior potentials. Therefore, the potential V_i is given by

$$V_i(\lambda_1,\lambda_2,\lambda_3) = \sum_{n=0}^{\infty}\sum_{p=1}^{2n+1} A_{(n,p)}^i \mathbb{E}_n^p(\lambda_1,\lambda_2,\lambda_3) + \sum_{n=0}^{\infty}\sum_{p=1}^{2n+1} B_{(n,p)}^i \mathbb{F}_n^p(\lambda_1,\lambda_2,\lambda_3), \alpha_1^i \leq \lambda_1 \leq \alpha_1^{i-1}. \qquad (25)$$

where $A_{(n,p)}^i$ and $B_{(n,p)}^i$ are the coefficients of the n^{th} degree and p^{th} order terms, respectively, of the interior and exterior potential distribution of the i^{th} tissue layer. The values α_1^i denote the major semi-axis length of the i^{th} ellipsoidal interface. The boundary conditions at an interface between the i^{th} and $(i+1)^{th}$ tissue layer with conductivities σ_i, $\sigma_{(i+1)}$ and potentials V_i, $V_{(i+1)}$ respectively, are defined as

$$\sigma_i \nabla V_i(\mathbf{r}).e_n = \sigma_{(i+1)}\nabla V_{(i+1)}(\mathbf{r}).e_n, \mathbf{r} \in \Omega_i^{(i+1)} \qquad (26)$$

$$V_i(\mathbf{r}) = V_{(i+1)}(\mathbf{r}), \mathbf{r} \in \Omega_i^{(i+1)} \qquad (27)$$

where e_n is the unit vector normal to the interface and $\mathbf{r}$ is a point on the surface $\Omega_i^{(i+1)}$ separating the i^{th} and $(i+1)^{th}$ layer. While (27) states continuity of potential, (26) states continuity of current density at the interface; it can also be seen as the inability to pile up charge at the interface. At the outermost interface (i.e., air–skin interface) we have non conducting air on one side and skin tissue with conductivity σ_1 on the other; hence, (26) becomes $\sigma_1\nabla V_1.e_n = 0$. This further implies the signal is confined to within the body. Furthermore, from the fact that potential vanishes at infinity, we have $\lim_{\mathbf{r}\to\infty} V_0(\mathbf{r}) = 0$.

Note that all but the third layer (muscle layer) do not contain any source. Hence (25) applies to all the layers except $i = 3$. Beginning from the exterior (air layer), the potential will only have the exterior form (i.e., $A_{(n.p)}^0 = 0$). Thus,

$$V_0(\lambda_1,\lambda_2,\lambda_3) = \sum_{n=0}^{\infty}\sum_{p=1}^{2n+1} B_{(n,p)}^0 \mathbb{F}_n^p(\lambda_1,\lambda_2,\lambda_3) \qquad (28)$$

for $\lambda_1 \geq \alpha_1^0$. The muscle layer contains the source, thus the potential expression includes the homogenous interior potential and the particular solution of the Poisson's equation. Denoting the particular solution by V_p, the potential distribution in the muscle tissue layer, i.e., $\alpha_1^3 \leq \lambda_1 \leq \alpha_1^2$, is then given by

$$V_3(\lambda_1,\lambda_2,\lambda_3) = V_p + \sum_{n=0}^{\infty}\sum_{p=1}^{2n+1} A_{(n,p)}^3 \mathbb{E}_n^p(\lambda_1,\lambda_2,\lambda_3) \qquad (29)$$

Let $\mathbf{r}_0$ be a vector from origin to the point where the current dipole $\mathfrak{M}$ is acting on. Then, the particular solution of the Poisson's equation for the potential, V_p, at any point referenced by vector $\mathbf{r}$ from the origin is given by [26],[33], [37]

This article has been accepted for publication in a future issue of this journal, but has not been fully edited. Content may change prior to final publication. Citation information: DOI 10.1109/TAP.2016.2559519, IEEE Transactions on Antennas and Propagation

$$V_p(\mathbf{r}) = -\frac{1}{4\pi\sigma_3}\mathfrak{M}\cdot\nabla_{\mathbf{r}_0}\frac{1}{|\mathbf{r}-\mathbf{r}_0|} \tag{30}$$

where the operation $\nabla_{\mathbf{r}_0}$ is the gradient with respect to $\mathbf{r}_0$. Now, let us replace the term $\frac{1}{|\mathbf{r}-\mathbf{r}_0|}$ with its ellipsoidal expansion;

$$\frac{1}{|\mathbf{r}-\mathbf{r}_0|} = \sum_{n=0}^{\infty}\sum_{p=1}^{2n+1}\frac{4\pi}{2n+1}\frac{1}{\gamma_n^p}\mathbb{E}_n^p(\lambda_{1_0},\lambda_{2_0},\lambda_{3_0})\mathbb{F}_n^p(\lambda_1,\lambda_2,\lambda_3) \tag{31}$$

where $(\lambda_{1_0},\lambda_{2_0},\lambda_{3_0})$ are ellipsoidal coordinates representing the point referenced by $\mathbf{r}_0$. Substituting (31) into (30) and (30) into (29), we have

$$V_3(\lambda_1,\lambda_2,\lambda_3) = \sum_{n=0}^{\infty}\sum_{p=1}^{2n+1}A_{(n,p)}^3\mathbb{E}_n^p(\lambda_1,\lambda_2,\lambda_3) + \sum_{n=0}^{\infty}\sum_{p=1}^{2n+1}\frac{\mathfrak{M}\cdot\nabla_{\mathbf{r}_0}\mathbb{E}_n^p(\lambda_{1_0},\lambda_{2_0},\lambda_{3_0})}{(2n+1)\sigma_3\gamma_n^p}\mathbb{F}_n^p(\lambda_1,\lambda_2,\lambda_3). \tag{32}$$

Thus, equating (32) with (25) for $i=3$, we can see that the value of $B_{(n,p)}^3$ is given by

$$B_{(n,p)}^3 = \frac{\mathfrak{M}\cdot\nabla_{\mathbf{r}_0}\mathbb{E}_n^p(\lambda_{1_0},\lambda_{2_0},\lambda_{3_0})}{(2n+1)\sigma_3\gamma_n^p}. \tag{33}$$

Applying the orthogonality property of ellipsoidal harmonics (23) and boundary conditions (26) and (27) into (28) and (29) at the four interfaces of Fig. 2, we have the following system of linear equations for each $i\in\{0,1,2,3\}$

$$A_{(n,p)}^i - A_{(n,p)}^{i+1} = (2n+1)I_n^p(\alpha_1^i)[B_{(n,p)}^{i+1} - B_{(n,p)}^i], \tag{34}$$

$$\sigma_i A_{(n,p)}^i - \sigma_{i+1}A_{(n,p)}^{i+1} = (2n+1)\Big[I_n^p(\alpha_1^i) - \frac{1}{C_{(n,p)}^i}\Big] \times\Big(\sigma_{i+1}B_{(n,p)}^{i+1} - \sigma_i B_{(n,p)}^i\Big). \tag{35}$$

where $C_{(n,p)}^i = E_n^p(\alpha_1^i)E_n^{p'}(\alpha_1^i)\alpha_2^i\alpha_3^i$ with $E_n^{p'}(\alpha_1^i)$ as the derivative of $E_n^p(\lambda_1)$ computed at $\lambda_1=\alpha_1^i$. Here, α_1^i is the major semi-axis length, and α_2^i and α_3^i are the other two semi-axes lengths of the i^{th} ellipsoid shown in Fig. 2.

Solving (34) and (35) with $A_{(n,p)}^0=0$ and $B_{(n,p)}^3$ as given in (33), the remaining coefficients are

$$B_{(n,p)}^1 = \frac{B_{(n,p)}^3}{\Big[\Big(1-\frac{\sigma_2}{\sigma_3}\Big)Q_n^pC_{(n,p)}^2 + \frac{W_n^p}{\sigma_3}\Big]},$$

$$A_{(n,p)}^1 = (2n+1)\Big[\frac{1}{C_{(n,p)}^0} - I_n^p(\alpha_1^0)\Big]B_{(n,p)}^1,$$

$$B_{(n,p)}^0 = \frac{B_{(n,p)}^1}{C_{(n,p)}^0 I_n^p(\alpha_1^0)},$$

$$A_{(n,p)}^2 = (2n+1)\Big[\frac{1}{C_{(n,p)}^0} + I_n^p(\alpha_1^1,\alpha_1^0) - \frac{W_n^pI_n^p(\alpha_1^1)}{\sigma_2}\Big]B_{(n,p)}^1,$$

$$B_{(n,p)}^2 = \frac{W_n^pB_{(n,p)}^1}{\sigma_2},$$

$$A_{(n,p)}^3 = (2n+1)\Big[Q_n^pB_{(n,p)}^1 - I_n^p(\alpha_1^2)B_{(n,p)}^3\Big],$$

$$B_{(n,p)}^4 = \Big(1-\frac{\sigma_3}{\sigma_4}\Big)C_{(n,p)}^3\Big[Q_n^pB_{(n,p)}^1 + I_n^p(\alpha_1^3,\alpha_1^2)B_{(n,p)}^3\Big] + \frac{\sigma_3}{\sigma_4}B_{(n,p)}^4,$$

$$A_{(n,p)}^4 = (2n+1)\Big[Q_n^pB_{(n,p)}^1 + I_n^p(\alpha_1^3,\alpha_1^2)B_{(n,p)}^3 - I_n^p(\alpha_1^3)B_{(n,p)}^4\Big]$$

where

$$I_n^p(\alpha_1^i,\alpha_1^j) = I_n^p(\alpha_1^i) - I_n^p(\alpha_1^j), \forall i,j\in\{0,1,2,3\},$$

$$W_n^p = (\sigma_2-\sigma_1)C_{(n,p)}^1\Big[\frac{1}{C_{(n,p)}^0} + I_n^p(\alpha_1^1,\alpha_1^0)\Big] - \sigma_1,$$

$$Q_n^p = \Big[\frac{1}{C_{(n,p)}^0} + I_n^p(\alpha_1^1,\alpha_1^0) + \frac{W_n^pI_n^p(\alpha_1^2,\alpha_1^1)}{\sigma_2}\Big]B_{(n,p)}^1.$$

This completes the derivation of the potential distribution at any point within the arm. The potential difference V_{Rx} sensed at the receiver is then given by the difference of the potentials at the receiver electrode locations as

$$V_{Rx} = V(r_1') - V(r_2'). \tag{36}$$

VI. Discussion

A. Received Potential Distribution

In the discussion of potential distribution and path loss, we use the human arm model given in Fig. 2 and the result in Section V-C. The various tissue layer thicknesses, on an arm of smallest semi-axis 43.5 mm, as taken by Amparo *et al* [21] are skin = 1.5 mm, fat = 8.5 mm, muscle = 27.5 mm, bone = 6 mm. Consider a transmitter injecting an rms current of 1 mA with its electrodes spaced by 5 mm located along the major semi-axis of the arm at 6.9 mm into the muscle tissue from the muscle-bone interface. The maximum electric potential developed along the axis of the dipole as a function of radial distance from the center is shown in Fig. 3.

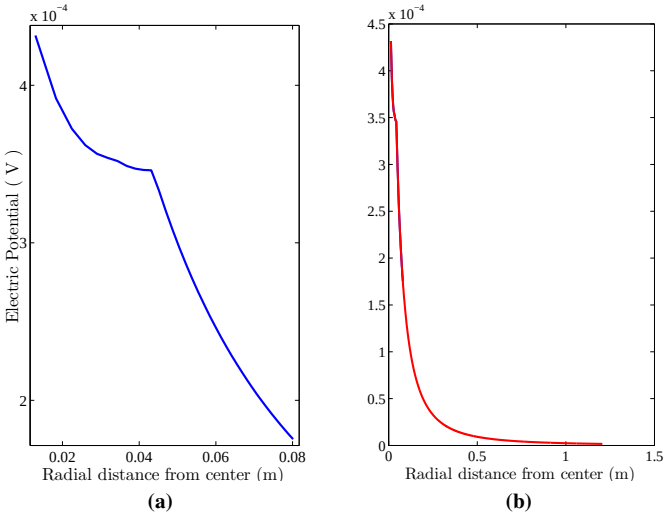

Fig. 3: Potential distribution at 600 KHz

From Fig. 3 (a), we can see that the potential decreases slowly starting from the transmitter location all the way to the surface of the skin (43.5 mm from the center). Clearly, the potential level is such that a receiver with electrodes on the surface of the skin along the two opposite sides of the current dipole can detect the transmission easily. However, the

This article has been accepted for publication in a future issue of this journal, but has not been fully edited. Content may change prior to final publication. Citation information: DOI 10.1109/TAP.2016.2559519, IEEE Transactions on Antennas and Propagation

potential rapidly decreases from the skin surface onwards. The zoomed out plot of the potential in Fig. 3 (b) shows that the potential falls so rapidly that we can safely assume the signal is confined to within the human body and is difficult to detect by an eavesdropping receiver not far from the body surface, suggesting the transmission technique is inherently secure. In

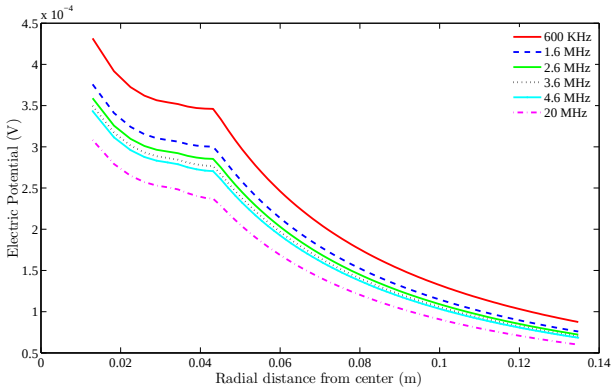

Fig. 4: Electric potential distribution at different frequencies

Fig. 4, we see that transmissions with lower frequency yield stronger electric potential inside the human body whereas the potential falls off quickly once it leaves the human body.

B. Path Loss

The path loss is defined as the attenuation of power as the signal travels from the transmitter to the receiver. Here, the received power is normalised to a 50 Ω load as shown in the two port network representation of galvanically coupled implant transceiver in Fig. 5.

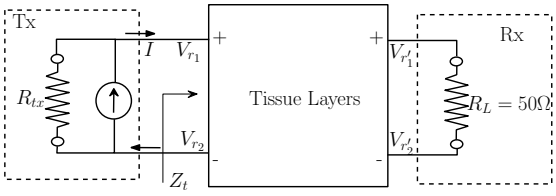

Fig. 5: Two port network representation of galvanically coupled implant communication.

In galvanic coupled implant communication, the channel is a direct load connected to the transmitter. Thus, it determines the amount of input power drawn from the transmitter. The transmitter injects the current I and sees an impedance of Z_t building up a potential $V_t = V_{r_1} - V_{r_2}$; using these, we can calculate the power input P_t. Also, using the 50 Ω load and the potential detected at the two electrodes of the receiver we can calculate the received power $P_r = (V_{r_1'} - V_{r_1'})^2/R_L$. Then, the path loss (PL) in dB is calculated as

$$PL = -10 \log \left(\frac{P_r}{P_t} \right). \tag{37}$$

Figure 6 shows the plot of path loss for various inter-electrode spacing of the transmitter where the receiver is located with fixed electrode-spacing on the surface of the

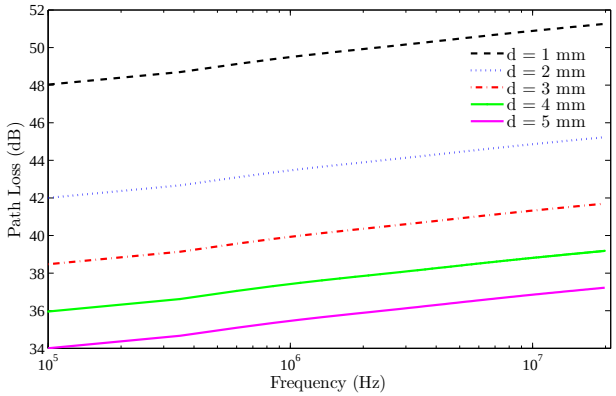

Fig. 6: Path loss for various inter-electrode spacing as a function of frequency for the communication scenario considered in Fig. 2.

skin. From this figure, we can see that the path loss increases with frequency. The trend followed by path loss characteristic of galvanic coupled implant communication is different from the *in vivo* measurements of the surface-to-surface intra-body communication [38]. This is due to the fact that the surface-to-surface communication and the implant-to-surface communications use different channels. In the surface-to-surface, the signal relies on the longitudinal path of the tissue layers where inner layers play a lesser role as frequency increases. However, for implant-to-surface communication, the signal

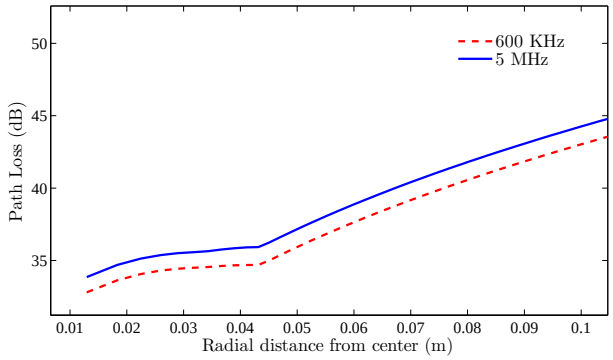

Fig. 7: Path loss as a function of separation distance between transmitter and receiver.

uses the transversal path penetrating all tissue layers all the way up to the skin. The mechanism of how tissue layers affect galvanically coupled implant communication is discussed in Section VI-D.

With regards to path loss, yet another important feature of intra-body communication is revealed in Fig. 7. Here, we see that path loss stays nearly constant (albeit slightly increasing) when the signal is within the body. However, once the signal leaves the skin at 43.5 mm radial distance, the path loss increases sharply.

C. Effect of Electrode Spacing: Implant Size

Assuming that the transmitter circuitry can be miniaturised to any size, the determinant factor for implant size is the electrode spacing. According to Fig. 6, it can be seen the

This article has been accepted for publication in a future issue of this journal, but has not been fully edited. Content may change prior to final publication. Citation information: DOI 10.1109/TAP.2016.2559519, IEEE Transactions on Antennas and Propagation

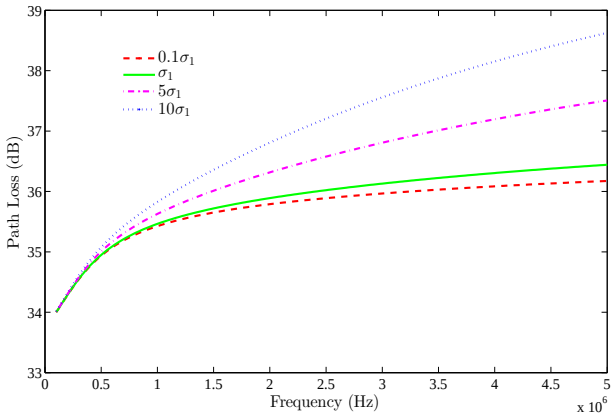

Fig. 8: Path loss for various values of conductivity of outer tissue layer. Here, σ_1 is the conductivity of skin.

path loss at the surface decreases by a factor of four when the electrode spacing doubles. Even for the 1 mm electrode spacing (the smallest shown in Fig. 6) the path loss for most frequency ranges below 10 MHz is limited to 40 dB range while the smallest side of the path loss for MICS based implants fall within 60 dB range [39].

In fact, frequencies in hundreds of megahertz such as the MICS 402-405 MHz with a bandwidth only of 300 kHz (which could be offered at a much lower frequency) will incur comparatively larger path loss due to the small skin (or penetration) depth (defined in Section VI-D) of tissue layers at high frequencies. The determinant parameter in frequency selection is then the bandwidth required for transmission and amount of interference in the frequency band. Another advantage of galvanically coupled implants is that, apart from the electrode spacing requirement, there is no need to use a radiating antenna which significantly influences the size of MICS type implants.

Our results suggest IBC based galvanically coupled implants operating at low frequencies are preferable for implant communication compared to radio wave based RF techniques.

D. Effect of Tissue Layers

The effect of tissue layers is contained in their thickness, conductivity and permittivity in frequencies of consideration. Channels that least attenuate electric field are preferable. This can be quantitatively described by skin depth (or penetration depth) which is defined as the distance at which an electromagnetic field is attenuated by a factor of $\frac{1}{e}$ (where e is the base of natural logarithm) as it passes through a medium of permittivity ϵ, permeability μ and conductivity σ. Skin depth δ at any frequency ($\omega = 2\pi f$) is given by

$$\delta = \frac{1}{\omega}\left[\frac{\mu\epsilon}{2}\left(\sqrt{1+\left(\frac{\sigma}{\epsilon\omega}\right)^2}-1\right)\right]^{-1/2}. \quad (38)$$

The smaller the skin depth the more the power gets attenuated and hence larger path loss. From (38), with the permittivity and conductivity of skin, fat, muscle and bone tissues according to (24) with coefficients from IT'IS [36], the skin depth is a decreasing function of frequency for all the tissues. Thus, the channel for implant-to-surface communication suffers increasing path loss with increasing conductivity as shown in Fig. 8. However, the rate at which the conductivity

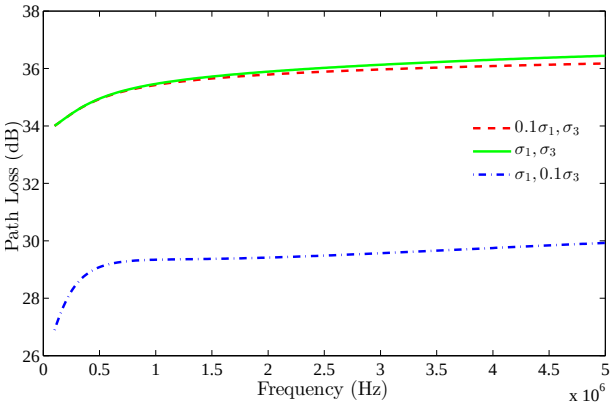

Fig. 9: Path loss for different values of conductivity of muscle (σ_3) and skin (σ_1) tissue layers.

increases or the permittivity decreases varies for different tissues. For example, up to 5 MHz the conductivity of skin is small but increases sharply while muscle tissue maintains a relatively steady conductivity across the frequency range.

The competing trends observed here are the conductivity and the penetration depth. Increased conductivity provides stronger conduction current while increased penetration depth provides stronger induced electric field. However, their effects are different for different tissue layers due to the value of conductivity and varying permittivity profiles with frequency. As seen in Fig. 9, the path loss is less sensitive to reduction in conductivity of skin tissue compared to that of muscle tissue.

Although reduced conductivity decreases path loss, the channel should also be conductive enough for the volume conduction according to (5). Thus, the potential distribution is as a result of a trade off between the penetration depth of the field and current conduction ability of each tissue layer.

The combination of tissue layers create a net impedance Z_t seen by the transmitter; and that determines the amount of power drawn by the channel (Fig. 10). Here, we can see that the transmit power is a decreasing function of frequency. This is due to the fact that as we go higher in frequency the impedance Z_t decreases. Besides, tissue thickness constitutes the percentage contribution of each tissue layer in the overall impedance Z_t. Since skin tissue is the thinnest of all tissue layers, its contribution is minimal. Thus, as we can see in Fig. 10, although the conductivity of skin tissue is increased and decreased by an order of magnitude, the amount of power input to the channel is not affected.

However, the case is not the same for the receiver (i.e., received power). In addition to the impedance, skin depth plays major role. Thus, as we can see in Fig. 11, when the conductivity of the skin is increased by an order of magnitude, the penetration depth decreases considerably and we observe large reduction in the received power especially at higher frequencies (as increasing frequency also further decreases penetration depth). But, when the conductivity of the skin is decreased by an order of magnitude, the improvement in

This article has been accepted for publication in a future issue of this journal, but has not been fully edited. Content may change prior to final publication. Citation information: DOI 10.1109/TAP.2016.2559519, IEEE Transactions on Antennas and Propagation

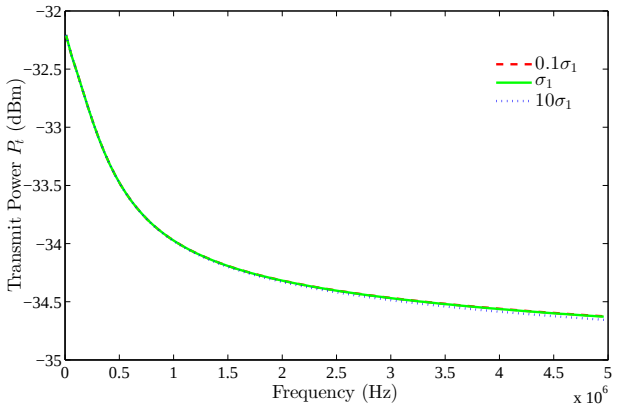

Fig. 10: Input power to the channel at the transmitter side for various values of conductivity of skin (σ_1) tissue layer.

received power is marginal. This is because, although the skin depth is increased, it is effectively counter acted by the increased resistance due to the reduction in conductivity.

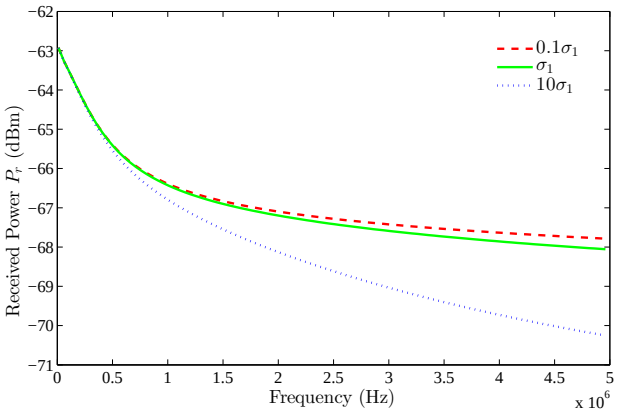

Fig. 11: Received power as a function of frequency for different values of conductivities of the skin (σ_1) tissue layer.

Another important observation here is that the power drawn is about -32 to -35 dBm which is a fraction of a microwatt. Taking such a small power, the receiver side of the channel still preserves about -63 to -68 dBm of the power as shown in Fig. 11. The average receiver sensitivity of the IEEE 802.15.6 standard for HBC receiver is -92.5 dBm; that is a lot smaller than the received power levels seen in Fig. 11. Thus, receivers compatible to the IEEE 802.15.6 standard can easily detect the received signal.

E. Potential Ratio and Optimal Frequencies

In a broad sense, the changes in received potential follow the variations of the path loss, i.e., when the path loss falls the received potential increases. However, received potential and path loss may take different patterns for implant communication in different body parts. The changing impedance of the channel as a function of frequency determines the amount of input power drawn by the channel. Thus, although the channel may offer small path loss, the impedance could be so small that small power is drawn and small potential is developed at the receiver side. In some cases, insignificant changes in path loss could mean significant changes in received potential. These are elegantly captured in our model. For example, refer to the implant communication setup in Fig. 15; as shown in Table I, when we increased the conductivity of the brain tissue by three times than used in Table III, the path loss did not change significantly while the received potential decreased by 35%.

TABLE I: Special case of Path Loss and Potential changes

Conductivity	Path Loss	Received Potential
σ_4	46.88 dB	89.8 μ V
$3\sigma_4$	46.69 dB	57 μ V

Thus, in addition to the path loss, we need to also look at the received potential since the actual input power at the transmitter depends on the channel itself. The ratio of receiver to input potential difference follows the trend shown in Fig. 12.

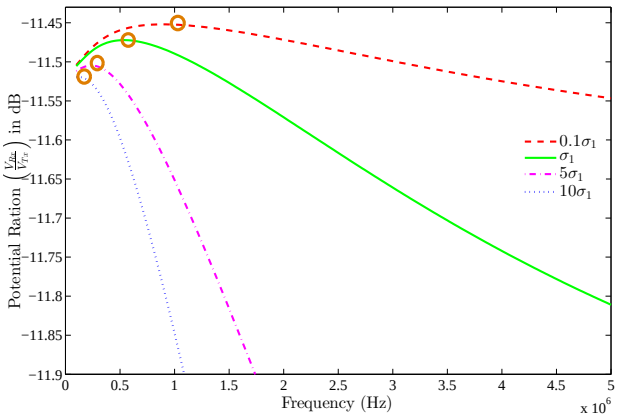

Fig. 12: Ratio of received and transmitter potential for different skin conductivity (σ_1). The circled points in the plot indicate the optimum frequencies at which the ratio is maximised.

Maximising the ratio of received potential to transmitted potential is equivalent to receiving the maximum possible potential at the receiver the channel can provide for the input potential at the transmitter. We refer to the frequencies where the received potential is maximised as optimum frequencies (shown circled in Fig. 12). These frequencies are determined by conductivity and permittivity profiles of the tissue strata. In general, the lower we make the conductivity the higher the optimal frequency is; for example, when skin conductivity is reduced by an order of magnitude, the optimal frequency is about 1.1 MHz. This is because the conductivity of skin is increasing with frequency and thus, the conductivity which optimizes path loss and impedance shifts to a higher frequency when we decrease the whole conductivity by a factor. Thus,the optimum frequency relies on the body composition and could range between several hundreds of kHz to a few MHz.

VII. Model Validation

A. Experimental Validation

The nature of the implant communication scenario makes it difficult, if not impossible, to conduct experiments in a

This article has been accepted for publication in a future issue of this journal, but has not been fully edited. Content may change prior to final publication. Citation information: DOI 10.1109/TAP.2016.2559519, IEEE Transactions on Antennas and Propagation

multilayered tissue phantom, especially when the experiment requires varying the distance between the transmitter and receiver. Thus, in our experimental validation, we used a homogenous aqueous muscle tissue phantom. Muscle is preferred as it constitutes 2/3 of the total tissue by volume.

Experimental Setup: Path loss measurements were conducted by transmitting signals through a phantom solution that is prepared to mimic conductivity and permittivity of muscle tissue at 13.56 MHz. The phantom solution is prepared according to the recipe given by Hagmann *et al* [40] shown in Table II. The aqueous solution is poured into a container shown in Fig. 13 with dimensions h = 12cm, b =9cm and w= 34 cm (the container roughly resembles a human arm).

TABLE II: Recipe for aqueous muscle tissue phantom at 13.56 MHz.

Frequency	Percentage of Weight			Properties	
(MHz)	Water	Glycine	NaCl	ϵ_r	σ (S/m)
13.56	79.4	20	0.58	145	0.6

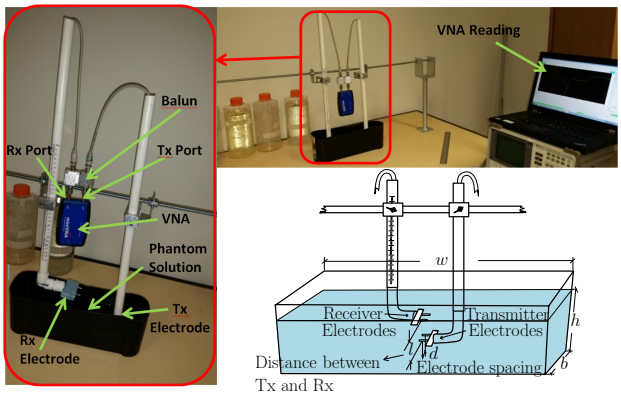

Fig. 13: Experimental setup for validation of proposed model.

The setup allows two degree of freedom for the electrodes, i.e., vertically and horizontally. By fixing the transmitter location, we can adjust the communication distances between the receiver and transmitter vertically and horizontally. In this particular experiment, the transmitter and receiver electrodes are aligned vertically and we adjusted the vertical distance by moving the receiver electrodes upwards.

A pair of shielded BNC cables is connected to the transmitter and receiver copper electrodes as shown in Fig. 13. Both the transmitter and receiver electrodes are prepared with 3 cm electrode spacing. A Vector Network Analyzer (VNA) is used to analyze the channel between the transmitter and receiver. The VNA we used is the Pro miniVNA (miniVNA Pro, Mini Radio Solutions Inc., Poland). Readings are recorded in a Laptop wirelessly connected to the VNA via BlueTooth. The transmitter and receiver electrodes are connected, respectively, to the DUT and DET ports of the VNA via a 50 Ohm Balun.

Measurement: Vertically, the transmitter is submerged at a depth of 6.7cm from the outer surface of the phantom solution (i.e., roughly at the center of the 12 cm high phantom solution). Horizontally, both the transmitter and receiver electrodes are located at the center of the 34 cm long phantom solution. The transmitter location is fixed and the vertical position of the receiver electrodes is varied; then the path loss readings were

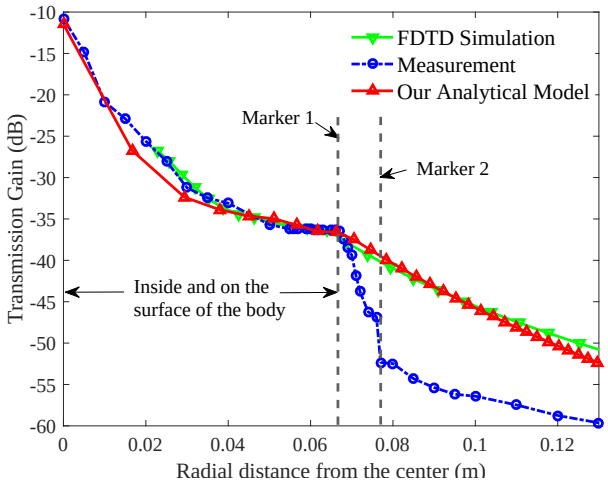

Fig. 14: Comparison of our model with measurement and simulation.

taken. The minVNA sweeps signals with frequencies 100 kHz to 200 MHz and measure the path loss at each frequency. By readjusting the distance, at each distance, 5 transmission gain measurements were taken (only those corresponding to 13.67 MHz were extracted). The path loss in dB is the negative of the transmission gain in dB. These results are averaged to determine average measured path loss at the corresponding communication distance.

We have also conducted a Finite Difference Time Domain (FDTD) simulation using SMECADx software for the same setting. For an implant-to-implant or implant-to-surface communication setting, the receiver can either be another implant or mounted on the surface of the skin. Thus, our region of interest (ROI) is the region inside and on the surface of the body. For this region, up to 6.7 cm radial distance from the center (i.e., marker 1 in Fig. 14), our analytical model and the FDTD simulation fit the measurement reasonably well as shown in Fig. 14. However, as we leave the surface of the skin, the measured path loss is larger than predicted by our model and the FDTD simulation, although the trend is similar after marker 2.

We believe the discrepancy outside the body is mainly due to the electrode contact impedance which is not considered in our model and the FDTD simulation. Insightful study on contact impedance in galvanic and capacitive electrodes surrounded by volumes of variable conductivity and permittivity profiles is presented in [41]. Inside the body, the receiver electrodes are connected and surrounded by a conducting tissue where both the conduction and induced currents exist; hence, the contact established is similar to metal-to-electrolyte contact [42], [43]. As such, compared to outside the body, the electrode contact impedance up to the surface is small and its effect on the path loss can be assumed negligible. This explains the fact that our model fits the measurement inside and on the surface of the body. On the other hand, outside the body the conduction current vanishes and the receiver electrodes stay in the air. Hence, the electrodes measure a high impedance which can not be ignored. This contact impedance increases as the electrodes move away from a conducting body. Hence,

This article has been accepted for publication in a future issue of this journal, but has not been fully edited. Content may change prior to final publication. Citation information: DOI 10.1109/TAP.2016.2559519, IEEE Transactions on Antennas and Propagation

the measured path loss increases at a larger gradient than modeled between vertical marker 1 and maker 2 as shown in in Fig. 14. After some distance (i.e., far enough for the conducting tissues to least affect the electrode contacts), the contact impedance does not change considerably. Thus, after marker 2, the measured path loss roughly takes slower slope as predicted by the FDTD and our model.

B. Comparison of the Model with Existing Work

We further compared our model with existing experimental results conducted by Sun *et al* [13]. Sun *et al* [13] used a simplified homogeneous spherical model and conducted experiments by inserting an implant inside the brain tissue of anesthetized pig. A current of 40 μA was injected by a dipole with the anode and the cathode separated by 1.4 cm. The overall radius of the head was taken as 7.5 cm and a homogeneous conductivity of 0.45 $\mathrm{m}^{-1}\cdot\Omega^{-1}$ was used.

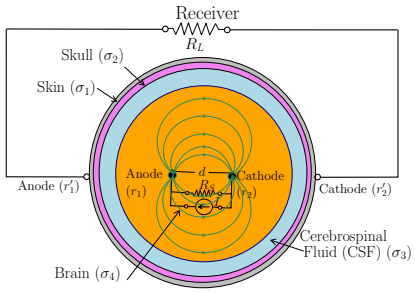

Fig. 15: Multilayered ellipsoidal approximation of head.

TABLE III: Potential difference detected at the receiver

	Homologous sphere [13]	Multilayered sphere [44]	Measured [13]	This work
V	105 μV	88 μV	90.72 μV	89.8 μV
$\%\Delta$	15.74 %	3.00 %	0 %	1.01 %

By changing our setup, as shown in Fig. 15, and recalculating the potential, we compared our result to previously reported values in Table III. Here, V refers to electric potential and $\%\Delta$ refers to the percentage error of the potential calculated using our model and other models with respect to the measured value [13]. The complex conductivities of tissues in Fig. 15 again were referred from [36]. Table III shows our model predicts the measured values with good accuracy demonstrating that it can be applied to any part of human body.

In summary, our model describes the signal reception in the ROI (i.e., by another implant or a wearable receiver). The fact that electrode contact impedance is large outside the body further strengthens the claim that the IBC signal is confined to within and on the body. Although the region away from the skin is not included in the ROI, inclusion of contact impedance into our model is an interesting problem for future work.

VIII. Conclusion

In this paper we have presented a new analytical model of galvanically couple intra-body communication as an alternative implant communication. The model is geometrically versatile to be used in any part of human body. Our model captures the electromagnetic effect of tissue layers, size and depth of the implant on input and received power, path loss, received potential and potential ratio. The predicted path loss at the surface is between 30-40dB for the frequency range of interest which coincides with empirical results previously reported. The model shows that galvanically coupled implant communication is not only feasible but possesses a better path loss characteristics and a potentially large degree of miniaturisation. Our discussion analysed tissue effects in depth and provided insight to applying the model to different parts of the body.

Appendix A
Lamé's functions of First kind E_n^p

Lamé's functions $E_n^p(\rho)$ for degree $n \leq 3$ and order $p \in \{1, 2, .., 2n+1\}$ where $h_j, \forall j \in \{1, 2, 3\}$ are semi-axis distances are given as follows

$$
\begin{aligned}
&E_0^1(\rho) = 1,\ E_1^1(\rho) = \rho,\\
&E_1^2(\rho) = \sqrt{|\rho^2 - h_3^2|}, E_1^3(\rho) = \sqrt{|\rho^2 - h_2^2|},\\
&E_2^1(\rho) = \rho^2 - \frac{1}{3}\left[(h_3^2+h_2^2) - \sqrt{(h_3^2+h_2^2)^2 - 3h_3^2h_2^2}\right],\\
&E_2^2(\rho) = \rho^2 - \frac{1}{3}\left[(h_3^2+h_2^2) + \sqrt{(h_3^2+h_2^2)^2 - 3h_3^2h_2^2}\right],\\
&E_2^3(\rho) = \rho\sqrt{|\rho^2 - h_3^2|},\ E_2^4(\rho) = \rho\sqrt{|\rho^2 - h_2^2|},\\
&E_2^5(\rho) = \sqrt{|(\rho^2 - h_3^2)(\rho^2 - h_2^2)|},\\
&E_3^1(\rho) = \rho^3 - \frac{\rho}{5}\left[2(h_3^2+h_2^2) - \sqrt{4(h_3^2+h_2^2)^2 - 15h_3^2h_2^2}\right],\\
&E_3^2(\rho) = \rho^3 - \frac{\rho}{5}\left[2(h_3^2+h_2^2) + \sqrt{4(h_3^2+h_2^2)^2 - 15h_3^2h_2^2}\right],\\
&E_3^3(\rho) = \sqrt{|\rho^2 - h_3^2|}\\
&\qquad\times\left(\rho^2 - \frac{1}{5}\left[h_3^2 + 2h_2^2 - \sqrt{(h_3^2+2h_2^2)^2 - 5h_3^2h_2^2}\right]\right),\\
&E_3^4(\rho) = \sqrt{|\rho^2 - h_3^2|}\\
&\qquad\times\left(\rho^2 - \frac{1}{5}\left[h_3^2 + 2h_2^2 + \sqrt{(h_3^2+2h_2^2)^2 - 5h_3^2h_2^2}\right]\right),\\
&E_3^5(\rho) = \sqrt{|\rho^2 - h_2^2|}\\
&\qquad\times\left(\rho^2 - \frac{1}{5}\left[2h_3^2 + h_2^2 - \sqrt{(2h_3^2+h_2^2)^2 - 5h_3^2h_2^2}\right]\right),\\
&E_3^6(\rho) = \sqrt{|\rho^2 - h_2^2|}\\
&\qquad\times\left(\rho^2 - \frac{1}{5}\left[2h_3^2 + h_2^2 + \sqrt{(2h_3^2+h_2^2)^2 - 5h_3^2h_2^2}\right]\right),\\
&E_3^7(\rho) = \rho\sqrt{|(\rho^2 - h_3^2)(\rho^2 - h_2^2)|}.
\end{aligned}
$$

Appendix B
Orthogonality Normalisation constants γ_n^p

Normalisation constants γ_n^p for degree $n \leq 3$, order $p \in \{1, 2, .., 2n+1\}$ and semi-axis distances h_j are given as

$$
\begin{aligned}
&\gamma_0^1 = 4\pi,\ \gamma_1^1 = \frac{4\pi h_3^2 h_2^2}{3},\ \gamma_1^2 = \frac{4\pi h_3^2(h_2^2 - h_3^2)}{3},\\
&\gamma_1^3 = \frac{4\pi h_3^2(h_3^2 - h_3^2)}{3},
\end{aligned}
$$

This article has been accepted for publication in a future issue of this journal, but has not been fully edited. Content may change prior to final publication. Citation information: DOI 10.1109/TAP.2016.2559519, IEEE Transactions on Antennas and Propagation

$$\gamma_2^1 = \frac{16\pi}{405}\Big[2h_3^8 + 2h_2^8 - 4h_3^6h_2^2 - 4h_3^2h_2^6 + 6h_3^2h_2^4 + \sqrt{h_3^4 + h_2^4 - h_3^2h_2^2}(-2h_3^6 - 2h_2^6 + 3h_3^4h_2^2 + 3h_3^2h_2^4)\Big],$$

$$\gamma_2^2 = \frac{16\pi}{405}\Big[2h_3^8 + 2h_2^8 - 4h_3^6h_2^2 - 4h_3^2h_2^6 + 6h_3^2h_2^4 - \sqrt{h_3^4 + h_2^4 - h_3^2h_2^2}(-2h_3^6 - 2h_2^6 + 3h_3^4h_2^2 + 3h_3^2h_2^4)\Big],$$

$$\gamma_2^3 = \frac{4\pi h_3^4h_2^2(h_2^2 - h_3^2)}{15},\ \gamma_2^4 = \frac{4\pi h_3^2h_2^4(h_2^2 - h_3^2)}{15},$$

$$\gamma_2^5 = \frac{4\pi h_3^2h_2^2(h_2^2 - h_3^2)^2}{15},$$

$$\gamma_3^1 = \frac{16\pi h_3^2h_2^2}{13125}\Big[16h_3^8 + 16h_2^8 - 36h_3^6h_2^2 - 36h_3^2h_2^6 + 46h_3^4h_2^4 + \sqrt{4h_3^2 + 4h_2^4 - 7h_3^2h_2^2}(-8h_3^6 - 8h_2^6 + 11h_3^4h_2^2 + 11h_3^2h_2^4)\Big],$$

$$\gamma_3^2 = \frac{16\pi h_3^2h_2^2}{13125}\Big[16h_3^8 + 16h_2^8 - 36h_3^6h_2^2 - 36h_3^2h_2^6 + 46h_3^4h_2^4 + \sqrt{4h_3^2 + 4h_2^4 - 7h_3^2h_2^2}(8h_3^6 + 8h_2^6 - 11h_3^4h_2^2 - 11h_3^2h_2^4)\Big],$$

$$\gamma_3^3 = \frac{16\pi h_3^2h_1^2}{13125}\Big[6h_3^8 + 16h_2^8 - 12h_3^6h_2^2 - 28h_3^2h_2^6 + 34h_3^4h_2^4 + \sqrt{h_3^4 + 4h_2^4 - h_3^2h_2^2}(-6h_3^6 - 8h_2^6 + 9h_3^4h_2^2 + 13h_3^2h_2^4)\Big],$$

$$\gamma_3^4 = \frac{16\pi h_3^2h_1^2}{13125}\Big[6h_3^8 + 16h_2^8 - 12h_3^6h_2^2 - 28h_3^2h_2^6 + 34h_3^4h_2^4 + \sqrt{h_3^4 + 4h_2^4 - h_3^2h_2^2}(6h_3^6 + 8h_2^6 - 9h_3^4h_2^2 - 13h_3^2h_2^4)\Big],$$

$$\gamma_3^5 = \frac{16\pi h_3^2h_1^2}{13125}\Big[16h_3^8 + 6h_2^8 - 28h_3^6h_2^2 - 12h_3^2h_2^6 + 34h_3^4h_2^4 + \sqrt{4h_3^2 + h_2^4 - h_3^2h_2^2}(-8h_3^6 - 6h_2^6 + 13h_3^4h_2^2 + 9h_3^2h_2^4)\Big],$$

$$\gamma_3^6 = \frac{16\pi h_3^2h_1^2}{13125}\Big[16h_3^8 + 6h_2^8 - 28h_3^6h_2^2 - 12h_3^2h_2^6 + 34h_3^4h_2^4 + \sqrt{4h_3^2 + h_2^4 - h_3^2h_2^2}(8h_3^6 + 6h_2^6 - 13h_3^4h_2^2 - 9h_3^2h_2^4)\Big],$$

$$\gamma_3^7 = \frac{4\pi h_3^4h_2^4h_1^4}{105}.$$

REFERENCES

[1] J. E. Ferguson and A. D. Redish, "Wireless communication with implanted medical devices using the conductive properties of the body," *Expert review of medical devices*, vol. 8, no. 4, pp. 427–433, 2011.

[2] Y. J. Heo and S. Takeuchi, "Towards smart tattoos: Implantable biosensors for continuous glucose monitoring," *Advanced healthcare materials*, vol. 2, no. 1, pp. 43–56, 2013.

[3] European Telecommunication Standard Institute (ETSI), "Electromagnetic compatibility and radio spectrum matters (ERM); short range devices (SRD); ultra low power active medical implants (ULP-AMI) and peripherals (ULP-AMI-P) operating in the frequency range 402 MHz to 405 MHz; part 1: Technical characteristics and test methods," in *European Standard (Telecommunications series)*, vol. V1.3.1, 2009.

[4] S. Hanna, "Regulations and standards for wireless medical applications," in *Proceedings of the 3rd international symposium on medical information and communication technology*, 2009, pp. 23–26.

[5] K. Bazaka and M. V. Jacob, "Implantable devices: issues and challenges," *Electronics*, vol. 2, no. 1, pp. 1–34, 2012.

[6] M. A. Hannan, S. M. Abbas, S. A. Samad, and A. Hussain, "Modulation techniques for biomedical implanted devices and their challenges," *Sensors*, vol. 12, no. 1, pp. 297–319, 2011.

[7] M. A. Hannan, S. Mutashar, S. A. Samad, and A. Hussain, "Energy harvesting for the implantable biomedical devices: issues and challenges," *Biomed. Eng. Online*, vol. 13, 2014.

[8] International Commission on Non-Ionizing Radiation Protection (ICNIRP), "Guidance for limiting exposure to time-varying electric, magnetic, and electromagnetic fields (up to 300 GHz)," in *Health Physics*, vol. 74, no. 4, Apr 1998, pp. 494–522.

[9] T. G. Zimmerman, "Personal area networks (PAN): nearfield intra-body communication," in *IBM Syst.*, vol. 35, no. 3-4, MA, USA, Apr. 1996, pp. 609–617.

[10] IEEE Standards Association and others, "IEEE standard for local and metropolitan area networks-part 15.6: wireless body area networks," *IEEE Std*, vol. 802, no. 6, 2012.

[11] T. Handa, S. Shoji, S. Ike, S. Takeda, and T. Sekiguchi, "A very low-power consumption wireless ECG monitoring system using body as a signal transmission medium," in *International Conference on Solid State Sensors and Actuators, 1997. TRANSDUCERS'97 Chicago.*, vol. 2. IEEE, 1997, pp. 1003–1006.

[12] D. P. Lindsey, E. L. McKee, M. L. Hull, and S. M. Howell, "A new technique for transmission of signals from implantable transducers," *IEEE Trans. Biomed. Eng.*, vol. 45, no. 5, pp. 614–619, 1998.

[13] M. Sun, M. Mickle, W. Liang, Q. Liu, and R. J. Sclabassi, "Data communication between brain implants and computer," *IEEE Trans. Neural Syst. Rehabil. Eng.*, vol. 11, no. 2, pp. 189–192, 2003.

[14] M. Sun, B. L. Wessel, W. Liang, P. Roche, Q. Liu, M. Mickle, R. J. Sclabassi *et al.*, "A volume conduction antenna for implantable devices," in *EMBS'03.*, vol. 4. IEEE, 2003, pp. 3356–3359.

[15] M. S. Wegmueller, S. Huclova, J. Froehlich, M. Oberle, N. Felber, N. Kuster, and W. Fichtner, "Galvanic coupling enabling wireless implant communications," *IEEE Trans. Instrum. Meas.*, vol. 58, no. 8, pp. 2618–2625, 2009.

[16] C. M. Furse and A. Chrysler, "A history & future of implantable antennas," in *APSURSI'14*. IEEE, 2014, pp. 527–528.

[17] C. Furse, R. Harrison, and F. Solzbacher, "Recent advances in biomedical telemetry," in *ICEAA'07*. IEEE, 2007, pp. 1026–1027.

[18] W. Besio and A. Prasad, "Analysis of skin-electrode impedance using concentric ring electrode," in *EMBS'06. 28th Annual International Conference of the IEEE*. IEEE, 2006, pp. 6414–6417.

[19] K. Hachisuka, Y. Terauchi, Y. Kishi, K. Sasaki, T. Hirota, H. Hosaka, K. Fujii, M. Takahashi, and K. Ito, "Simplified circuit modeling and fabrication of intrabody communication devices," *Sensors and actuators A: physical*, vol. 130, pp. 322–330, 2006.

[20] B. Kibret, M. Seyedi, D. T. H. Lai, and M. Faulkner, "Investigation of galvanic-coupled intrabody communication using the human body circuit model," in *IEEE J. Biomed. Health Inform*, vol. 18, no. 4, July 2014, pp. 1196–1206.

[21] M. Amparo Callejon, J. Reina-Tosina, D. Naranjo-Hernández, and L. M. Roa, "Galvanic coupling transmission in intrabody communication: A finite element approach," *IEEE Trans. Biomed. Eng.*, vol. 61, no. 3, pp. 775–783, 2014.

[22] J. A. Ruiz, J. Xu, and S. Shimamoto, "Propagation characteristics of intra-body communications for body area networks," in *3rd IEEE CCNC 2006.*, vol. 1. IEEE, 2006, pp. 509–513.

[23] J. Bae, H. Cho, K. Song, H. Lee, and H.-J. Yoo, "The signal transmission mechanism on the surface of human body for body channel communication," in *IEEE Trans. Microw. Theory Techn.*, vol. 60, no. 3, March 2012, pp. 582–593.

[24] S. H. Pun, Y. M. Gao, P. Mak, M. Vai, M. Du *et al.*, "Quasi-static modeling of human limb for intra-body communications with experiments," *IEEE Trans. Info. Tech. in Biomed.*, vol. 15, no. 6, pp. 870–876, 2011.

[25] D. Dechambre, "Computation of ellipsoidal gravity field harmonics for small solar system bodies," *Electrical Engineering-Systems in The University of Michigan*, 2000.

[26] F. Kariotou, "Electroencephalography in ellipsoidal geometry," *Journal of Math. Analysis and Applications*, vol. 290, no. 1, pp. 324–342, 2004.

[27] G. Dassios and F. Kariotou, "Magnetoencephalography in ellipsoidal geometry," *Journal of Math. Physics*, vol. 44, no. 1, pp. 220–241, 2003.

[28] C. E. Tenke and J. Kayser, "Generator localization by current source density (CSD): implications of volume conduction and field closure at intracranial and scalp resolutions," *Clinical neurophysiology*, vol. 123, no. 12, pp. 2328–2345, 2012.

[29] S. B. Rutkove, "Introduction to volume conduction," *The clinical neurophysiology primer*, vol. 388, p. 43, 2007.

[30] R. Plonsey and D. B. Heppner, "Considerations of quasi-stationarity in electrophysiological systems," *The Bulletin of mathematical biophysics*, vol. 29, no. 4, pp. 657–664, 1967.

[31] J. H. Nagel, "Biopotential amplifiers," *Bronzino JD: Biomedical engineering hand book, 2nd ed., Springer-Verlag New York*, pp. 70–1, 2000.

[32] G. Dassios, *Ellipsoidal harmonics: theory and applications*. Cambridge University Press, 2012, vol. 146.
[33] D. B. Geselowitz, "On bioelectric potentials in an inhomogeneous volume conductor," *Biophysical journal*, vol. 7, no. 1, p. 1, 1967.
[34] M. Lynn and W. Timlake, "Multiple wielandt deflations in the numerical solution of singular integral equations of potential theory," in *Proceedings of the 23rd ACM national conference*, 1968, pp. 481–484.
[35] S. Gabriel, R. Lau, and C. Gabriel, "The dielectric properties of biological tissues: Iii. parametric models for the dielectric spectrum of tissues," *Physics in medicine and biology*, vol. 41, no. 11, p. 2271, 1996.
[36] IT'IS Foundation. (2013, Feb.) "Tissue Properties Database V2.3''. Thermal and dielectric properties V2.3(Excel).xls. [Online]. Available: http://www.itis.ethz.ch/virtual-population/tissue-properties/downloads/database-v2-3/
[37] D. B. Geselowitz, "On the theory of the electrocardiogram," *Proceedings of the IEEE*, vol. 77, no. 6, pp. 857–876, 1989.
[38] Y. Song, Q. Hao, K. Zhang, M. Wang, Y. Chu, and B. Kang, "The simulation method of the galvanic coupling intrabody communication with different signal transmission paths," *IEEE Trans. Instrum. Meas.*, vol. 60, no. 4, pp. 1257–1266, 2011.
[39] K. L.-L. Roman, G. Vermeeren, A. Thielens, W. Joseph, and L. Martens, "Characterization of path loss and absorption for a wireless radio frequency link between an in-body endoscopy capsule and a receiver outside the body," *EURASIP Journal on Wireless Communications and Networking*, vol. 2014, no. 1, pp. 1–10, 2014.
[40] M. Hagmann, R. Levin, L. Calloway, A. Osborn, and K. Foster, "Muscle-equivalent phantom materials for 10-100 MHz," *IEEE Trans. on Microwave Theory and Tech.*, vol. 40, no. 4, pp. 760–762, 1992.
[41] A. Hördt, P. Weidelt, and A. Przyklenk, "Contact impedance of grounded and capacitive electrodes," *Geophysical Journal International*, vol. 193, no. 1, pp. 187–196, 2013.
[42] L. Geddes and R. Roeder, "Criteria for the selection of materials for implanted electrodes," *Annals of biomedical engineering*, vol. 31, no. 7, pp. 879–890, 2003.
[43] I. A. Hokajärvi, "Electrode contact impedance and biopotential signal quality," *Thesis, Tampere University of Technology, Finland*, 2012.
[44] M. Sun, "An efficient algorithm for computing multishell spherical volume conductor models in EEG dipole source localization," *IEEE Trans. Biomed. Eng.*, vol. 44, no. 12, pp. 1243–1252, 1997.

Assefa K. Teshome (M'11) received the B.Sc. degree in Electrical Engineering from Bahir Dar University, Bahir Dar, Ethiopia in 2003; the M. Tech. degree in Electrical Engineering from Indian Institute of Technology – Madras (IIT–Madras), Chennai, India in 2007 and the M. Eng. (research) degree in Telecommunications Engineering from the University of South Australia, Adelaide, Australia in 2013. He is currently working toward the Ph.D. degree in the College of Engineering and Science, Victoria University, Melbourne, Australia. His research interests include signal propagation and communication models for body area networks (BAN) in addition to signal processing techniques for Biomedical and Biometric applications.

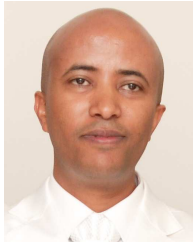

Behailu Kibret Behailu Kibret (M'11) received the B.Sc. degree in Electrical Engineering from Bahir Dar University, Bahir Dar, Ethiopia, in 2005; and the Ph.D. degree in Electrical Engineering from Victoria University, Melbourne Australia, in 2016. He is currently working as a Research Fellow in Monash University, Melbourne, Australia. His research interest includes electromagnetics, antennas and body area networks.

Daniel T. H. Lai (M'06) received the B.Eng (Hons.) and the Ph.D. degree in electrical and computer systems from Monash University, Melbourne, Australia.

He was a Research Fellow in the University of Melbourne and Victoria University (2007-2010). He is currently with the College of Engineering and Science, Victoria University. He has more than 80 peer-reviewed publications and is a current reviewer for several international journals. He is also actively involved in organization of several workshops and international conferences. His research interests include new sensing and communication technologies for body area networks.